Single InAs Nanowire Room-Temperature Near-Infrared Photodetectors

Jinshui Miao,[†,#] Weida Hu,[†,#,*] Nan Guo,[†,#] Zhenyu Lu,[†,#] Xuming Zou,[‡] Lei Liao,[‡,*] Suixing Shi,[†,#] Pingping Chen,[†,#] Zhiyong Fan,[§] Johnny C. Ho,[⊥] Tian-Xin Li,[†,#] Xiao Shuang Chen,[†,#,*] and Wei Lu[†,#]

[†]National Laboratory for Infrared Physics, Shanghai Institute of Technical Physics, Chinese Academy of Sciences, 500 Yutian Road, Shanghai 200083, China, [‡]Department of Physics and Key Laboratory of Artificial Micro- and Nano-structures of Ministry of Education, Wuhan University, Wuhan 430072, China, [§]Department of Electronic and Computer Engineering, Hong Kong University of Science and Technology, Hong Kong SAR, China, [⊥]Department of Physics and Materials Science, City University of Hong Kong, Hong Kong SAR, China, and [#]Synergetic Innovation Center of Quantum Information and Quantum Physics, University of Science and Technology of China, Hefei, Anhui 230026, China

ABSTRACT Here we report InAs nanowire (NW) near-infrared photodetectors having a detection wavelength up to ~1.5 μm. The single InAs NW photodetectors displayed minimum hysteresis with a high I_{on}/I_{off} ratio of 10^5. At room temperature, the Schottky−Ohmic contacted photodetectors had an external photoresponsivity of ~5.3×10^3 AW^{-1}, which is ~300% larger than that of Ohmic−Ohmic contacted detectors (~1.9×10^3 AW^{-1}). A large enhancement in photoresponsivity (~300%) had also been achieved in metal Au-cluster-decorated InAs NW photodetectors due to the formation of Schottky junctions at the InAs/Au cluster contacts. The photocurrent decreased when the photodetectors were exposed to ambient atmosphere because of the high surface electron concentration and rich surface defect states in InAs NWs. A theoretical model based on charge transfer and energy band change is proposed to explain this observed performance. To suppress the negative effects of surface defect states and atmospheric molecules, new InAs NW photodetectors with a half-wrapped top-gate had been fabricated by using 10 nm HfO$_2$ as the top-gate dielectric.
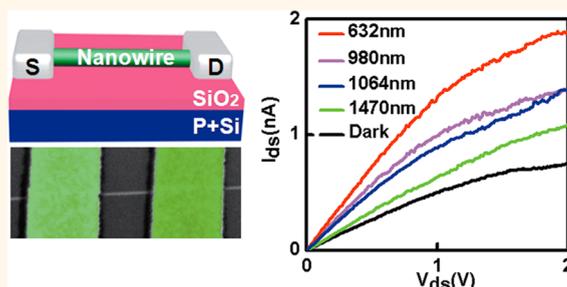
KEYWORDS: InAs nanowire · infrared photodetectors · half-wrapped top-gate · photoresponsivity · surface defect states

In the past few years, III−V semiconductor NWs have received considerable attention as potential building blocks for a variety of fundamental optical and electronic components, including radio frequency electronics, solar cells, photonic devices, and photodetectors.[1−8] For instance, ultrahigh photocurrent gain was achieved in GaN NW photodetectors, which was approximately 3 orders of magnitude higher than for thin film counterparts; the GaAs/AlGaAs core−shell NW photodetectors had a picosecond response time, showing its high-speed performance, and very high room-temperature mobility was also obtained in radial core−shell InAs/InP NWs.[9−11] Of particular interest in III−V semiconductor NWs is the InAs NW because of its high carrier mobility, narrow band gap for infrared detection, ease of Ohmic contact formation, and surface Fermi level pinning above the conduction band edge.[12−15]

According to the radio frequency response of InAs NW array field-effect transistors (FETs), the InAs NW can be used for ultrahigh frequency electronics.[1] It is also a promising candidate for ballistic transistors given its long bulk electron mean free path.[20,21] InAs NWs passivated by an Al$_2$O$_3$ dielectric show mobility enhancement and minimum hysteresis which are attributed to the reduction of surface trap density and surface recombination.[3] In addition, InAs NWs are very sensitive to chemical molecules and can be used as biochemical sensors due to their high surface electron concentration and rich surface defect states.[16−19,22] As a result, it is of particular importance to manipulate the surface defect states and chemical molecules to meet the applications of InAs NWs. However, most research mainly focuses on the electrical characteristics of InAs NWs.[1−5,11−13,19−26] To the best of our knowledge, no room-temperature InAs NW infrared
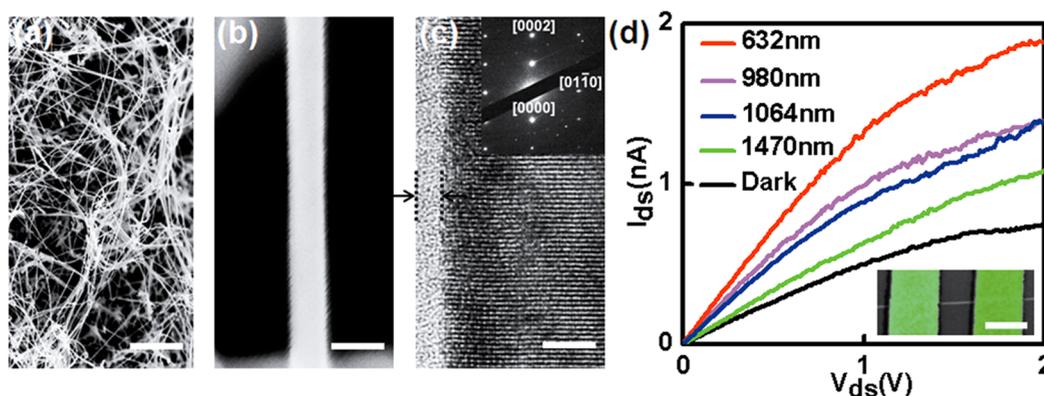
Figure 1. (a,b) SEM images of InAs NWs. The scale bar is 1 μm and 50 nm, respectively. (c) High-resolution TEM image and corresponding selected area electron diffraction (SAED) pattern (inset). The scale bar is 5 nm. (d) Photocurrent spectra of InAs NW near-infrared photodetectors changing from red to near-infrared light. The inset is the SEM image of a representative InAs NW photodetector. The scale bar is 1 μm.

photodetectors having a detection wavelength up to ~1.5 μm have been reported. Therefore, it is necessary to study the optoelectronic properties of InAs NWs in the infrared region, especially the effects of surface defect states and atmospheric molecules on its photoresponse.

InAs NWs used in this work were synthesized on GaAs (111)$_B$ substrates by the molecular beam epitaxy (MBE) technique. Room-temperature near-infrared photodetectors have been constructed with these as-grown single-crystalline structures. The source/drain (S/D) electrodes of the detectors were defined on each NW by electron-beam lithography (EBL), metallization, and lift-off processes. This study investigated the photoresponse of Schottky−Ohmic and Ohmic−Ohmic contacted InAs NW photodetectors. We also analyzed the effects of atmospheric molecules, metal-cluster decoration, and a HfO$_2$ passivation layer on the photoresponse. Furthermore, new InAs NW photodetectors with half-wrapped top-gate structures were introduced to suppress the negative effects of surface defect states and atmospheric molecules by employing the 10 nm HfO$_2$ as the top-gated dielectric. These devices are attractive for potential applications in integrated optoelectronic systems such as on-chip information communication and processing.

RESULTS AND DISCUSSION

The scanning electron microscope (SEM) images of InAs NWs indicate that they are very uniform with a length of ~10 μm (Figure 1a) and a diameter of ~40 nm (Figure 1b). The typical high-resolution transmission electron microscopy (HRTEM) image is presented in Figure 1c. It shows that the InAs NWs are relatively homogeneous without any obvious domain boundaries, demonstrating their single-crystalline nature. It also shows that the InAs NWs have a native oxide layer (L ~ 2 nm), which has already been demonstrated by previous work.[2] To further characterize the crystalline structure of the NWs, the selected area electron

diffraction (SAED) pattern of the same NW is shown in an inset of Figure 1c, indicating that the InAs NW has a wurtzite single-crystal structure with a dominate growth direction of [0001]. Figure 1d displays the photocurrent spectrum of a representative InAs NW near-infrared photodetector changing from red (λ ~ 632 nm) to near-infrared light (λ ~ 1.5 μm). It shows that the detector has a distinct photoresponse. The inset of Figure 1d shows the SEM image of the InAs NW near-infrared photodetector. Figure S1 (Supporting Information) presents the photoluminescence (PL) spectrum of InAs NWs which displays a wide peak around 3.4 μm.

To investigate the electrical properties of InAs NWs, FETs were fabricated on a P$^+$-Si/SiO$_2$ (300 nm) substrate. The Ohmic−Ohmic contacted FETs (inset, Figure 2a) were fabricated by employing metal Cr/Au (20 nm/40 nm) as S/D electrodes, while the Schottky−Ohmic contacted FETs (inset, Figure 2d) used metal Cr/Au (20 nm/40 nm) and Au (60 nm) as S/D electrodes, respectively. The representative NW FETs consist of a single InAs NW as the channel material with length of L ~ 7 μm and diameter of d ~ 40 nm, as depicted in the SEM images of Figure 2a,d (inset). Figure 2a,c presents the drain current *versus* gate voltage (I_{ds}−V_{gs}) transfer characteristics of Ohmic−Ohmic contacted FETs. The device displayed minimum hysteresis with a high I_{on}/I_{off} ratio of 10^5, which is much larger than the previous results,[12,23−26] as shown in Figure 2f. This is mainly attributed to the good single-crystalline nature of the InAs NW as well as the contacts of the devices.[2] Figure 2b depicts the I_{ds}−V_{ds} output characteristics of the same device. The linear I_{ds} behavior at low V_{ds} indicates the good Ohmic contacts between the InAs NW and metal Cr/Au electrodes. Figure 2d shows the I_{ds}−V_{gs} transfer characteristics of Schottky−Ohmic contacted InAs NW FETs. The diode-like I_{ds}−V_{ds} curves (Figure 2e) show that the contacts at the two electrodes are different; one side has a higher Schottky barrier (SB), while the other side has a lower or zero height SB,
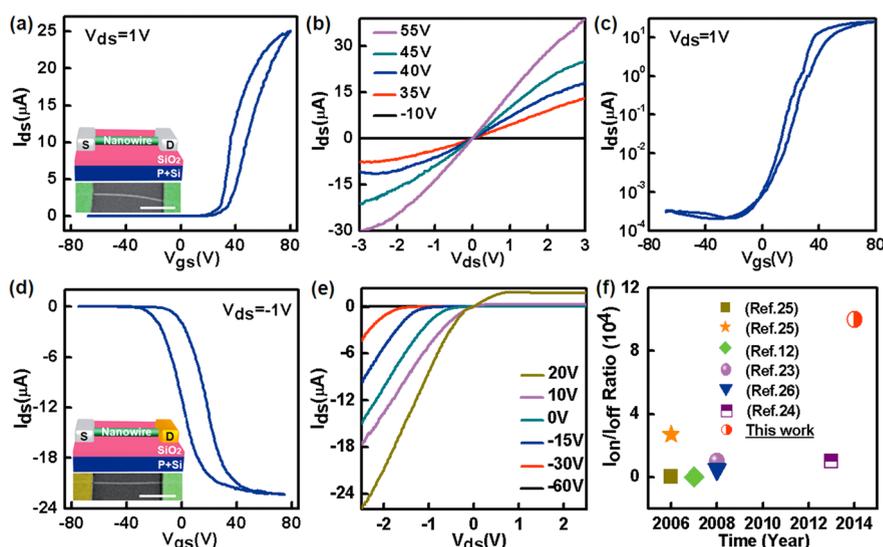
Figure 2. (a) I_{ds} *versus* V_{gs} curve of Ohmic−Ohmic contacted InAs NW FETs. The inset is the schematic and SEM image of Ohmic−Ohmic contacted InAs NW FETs. The scale bar is 4 μm. (b) Family of I_{ds} *versus* V_{ds} curves for various gate biases. (c) Logarithmic curve of panel a. (d) I_{ds} *versus* V_{gs} curve of Schottky−Ohmic contacted InAs NW FETs. The inset is the schematic and SEM image of Schottky−Ohmic contacted InAs NW FETs. The scale bar is 4 μm. (e) Family of I_{ds} *versus* V_{ds} curves for various gate biases. (f) I_{on}/I_{off} ratios of InAs NW FETs from previous publications and our work. All of these measurements were conducted in the vacuum conditions at room temperature.

similar to Ohmic contact. Figure S2 and Figure S3 (Supporting Information) display the top-gated Ohmic−Ohmic and Schottky−Ohmic contacted InAs NW FETs in the ambient atmosphere. The devices exhibited good electrical properties with a 10 nm HfO_2 dielectric. The high saturation current and conductance of the InAs NWs arise from their high electron mobility, which can be estimated by using the equation[34,37]

$$\mu_{FE} = \frac{g_m L^2}{C_g V_{ds}} \quad (1)$$

in the linear operation regime. Here the channel length L is ∼7 μm and $g_m = dI_{ds}/dV_{gs}$ is the NW device transconductance. C_g is the back-gate capacitance which can be deduced based on the cylinder on-plane model:[34,37]

$$C_g = \frac{2\pi\varepsilon_0\varepsilon_r L}{\ln(4h/d)} \quad (2)$$

where ε_r is the dielectric constant of SiO_2, ε_0 is the permittivity of free space, $h \sim 300$ nm is the thickness of the SiO_2 layer, and $d \sim 40$ nm is the InAs NW diameter. The calculated carrier mobility is ∼2000 cm^2 V^{-1} s^{-1}, which is comparable to previous results reported by other research groups.[3,26]

To shed light on the mechanism of Schottky−Ohmic and Ohmic−Ohmic contacted InAs NW FETs, energy band diagrams are introduced in this section, as depicted in Figure 3. Since the Fermi level (E_F) of intrinsically n-type InAs is ∼5.0 eV, which is higher than the work function of metal Cr ($\psi_1 \sim 4.5$ eV), the metal Au has a work function of $\psi_2 \sim 5.4$ eV. Therefore, the negative work function difference ($W_{Cr} - W_{InAs}$) induces a downward band-bending at the InAs NW/Cr
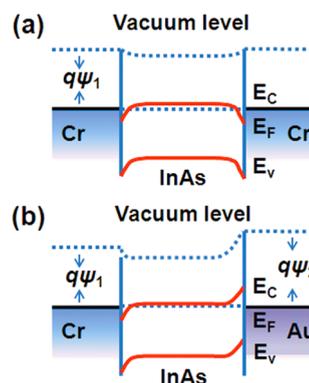

Figure 3. (a) Cr/InAs/Cr energy band diagram. (b) Cr/InAs/Au energy band diagram. The work function of Cr is ∼4.5 eV. The work function of InAs is ∼5.0 eV. The work function of Au is ∼5.4 eV.

contacts (Figure 3a), thus forming Ohmic contacted electrodes. The positive work function difference ($W_{Au} - W_{InAs}$) induces an upward band-bending at the InAs NW/Au contacts (Figure 3b), thus forming Schottky contacted electrodes. The height of Schottky barrier is $q\psi_B = q(\psi_2 - \chi)$, where χ is the InAs NW electron affinity. The Schottky−Ohmic contacted NW FETs exhibit much greater drain current when the SB is reversely biased than when it is forward biased, as depicted in Figure 2e.

The photoresponse of InAs NW photodetectors is explored by investigating their output characteristics of photocurrent and switching behavior at room temperature. The inset of Figure 4a illustrates the SEM image of Ohmic−Ohmic or Schottky−Ohmic contacted InAs NW photodetectors. The photoresponsivity of the Ohmic−Ohmic contacted photodetectors is
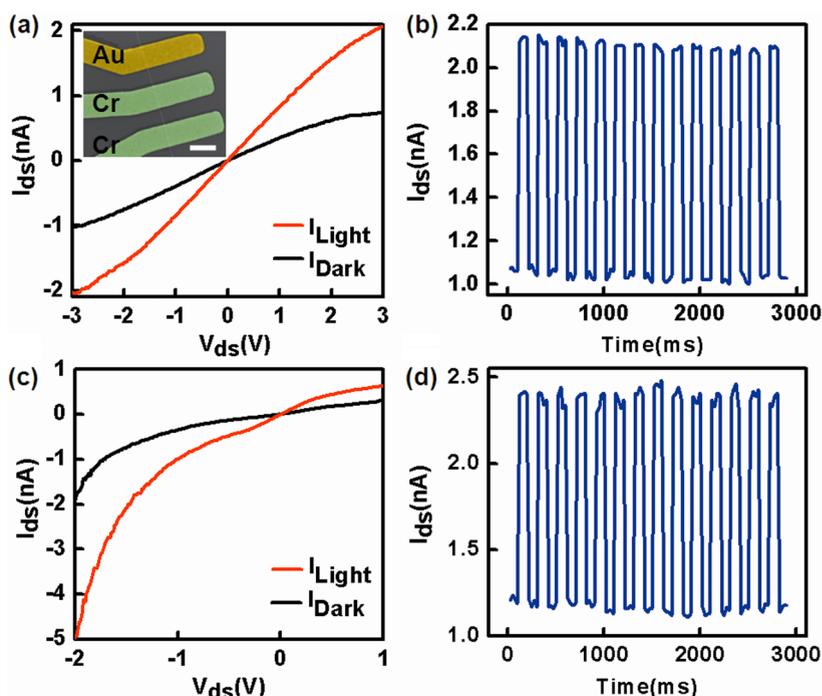
Figure 4. (a,b) Photoinduced I_{ds} *versus* V_{ds} curves and time-dependent photoresponse of Ohmic−Ohmic contacted InAs NW photodetectors. The inset is the SEM image of the device. The scale bar is 1 μm. (c,d) Photoinduced I_{ds} *versus* V_{ds} curves and time-dependent photoresponse of the Schottky−Ohmic contacted InAs NW photodetectors.

$\sim$1.9 $\times$ 10^3 AW^{-1}, as shown in Figure 4a. The photoresponsivity can be calculated by the following equation:[33]

$$R = \frac{I_{ph}}{PS} \tag{3}$$

where the I_{ph} is the photocurrent of the device, P is the average light power on InAs NW ($\sim$1 mW/cm^2), and S is the effective illuminated area. The photoresponse can also be observed in a dynamic way. The on−off photoswitching behavior (Figure 4b) is well retained even after 14 cycles. All of these results confirm the good stability of the InAs NW photodetectors. The photoresponsivity of Schottky−Ohmic contacted photodetectors is $\sim$5.3 $\times$ 10^3 AW^{-1}, which is $\sim$300% larger than that of Ohmic−Ohmic contacted devices ($\sim$1.9 $\times$ 10^3 AW^{-1}), as depicted in Figure 4c. This is attributed to the strong built-in electric field in the InAs NW/Au electrode Schottky junctions, thus efficiently separating the photon-generated electron−hole pairs or suppressing the recombination rate of photon-generated electron−hole pairs.[27] Furthermore, the migration of electrons to the electrode side and holes in the depletion layer reduces the local net charge density, thus, the built-in field is lowered, resulting in a reduced SB height.[28] Figure 4d shows the on−off photoswitching behavior of Schottky−Ohmic contacted InAs NW photodetectors.

InAs NWs are very sensitive to chemical molecules, due to excellent electronic transport performance, large surface-to-volume ratio, and the existence of an intrinsic electron accumulation layer.[17] Moreover, the rich defect states can facilitate electron transfers to molecules adsorbed on InAs NWs.[19] In this section, we studied the effects of atmospheric molecules and a HfO$_2$ passivation layer on optoelectronic properties of InAs NW photodetectors. The sample chamber was first pumped to a vacuum of 5 $\times$ 10^{-4} Pa to remove the ambient gases and moisture in the chamber. Figure 5a shows the schematic illustrations of InAs NW photodetectors with adsorbed atmospheric molecules (bottom image) or a 10 nm HfO$_2$ passivation layer (top image). Figure 5b presents the I_{ds}−V_{gs} transfer characteristics of the same photodetector in both atmosphere and vacuum conditions and with a 10 nm HfO$_2$ passivation layer. The hysteresis decreased when the detector was in the vacuum condition (black line, Figure 5b). The device had the least hysteresis with a 10 nm HfO$_2$ passivation layer (red line, Figure 5b). The on-current decreased after introducing atmospheric molecules (blue line, Figure 5c), and the device with the passivation layer had the largest on-current (red line, Figure 5c). The mobility and photocurrent also obeyed the same trend, as shown in Figure 5e,f. Due to the large surface-to-volume ratio of NWs and the Debye length, the electronic properties of NW FETs are strongly influenced by the scattering from surface states. The exposed interstitials at the NW surface yield a NW channel that is sensitive to ambient environment.[35,36] The HfO$_2$ passivation layer can reduce the device hysteresis by protecting the NW from the ambient environment and surface defect states, thus improving the device
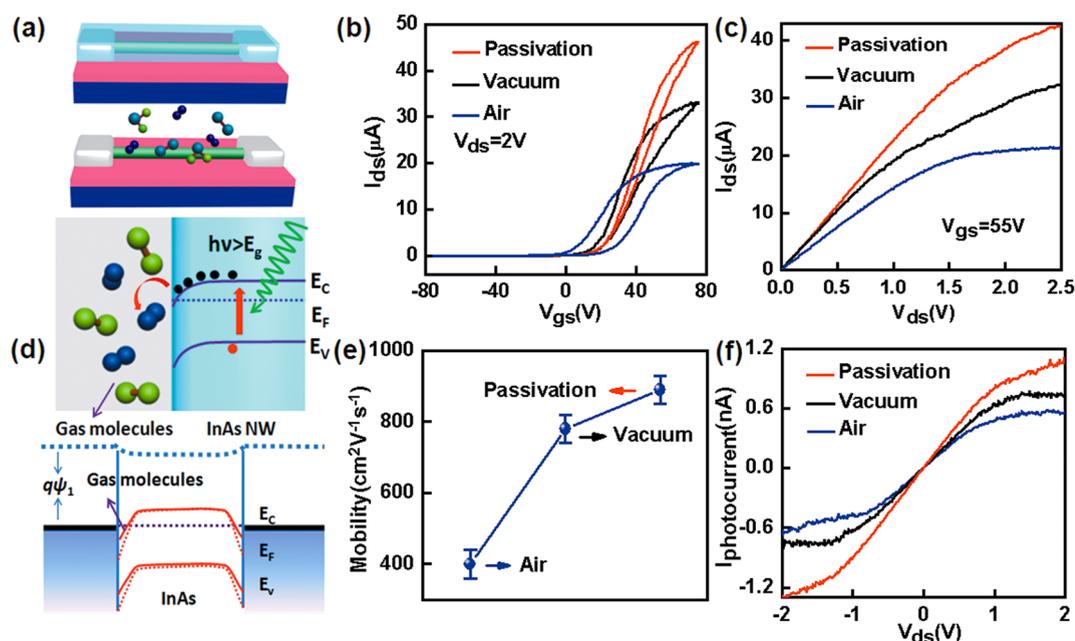
Figure 5. (a) Schematic of InAs NW photodetectors with or without a 10 nm HfO$_2$ passivation layer. (b) I_{ds} *versus* V_{gs} curves of InAs NW photodetectors. (c) I_{ds} *versus* V_{ds} curves of the same detector. (d) Theoretical models of the effects of atmospheric molecules. (e) Electron mobility changes of InAs NW photodetectors. (f) Photoresponse of the same InAs NW photodetectors.

performance.[29,35,36] Figure S4 (Supporting Information) shows the effects of N$_2$ and O$_2$ molecules on InAs NW array photodetectors, indicating that the photocurrent decreased after introducing the N$_2$ and O$_2$ molecules.

One possible explanation of the results presented above can be interpreted as the charge transfer mechanism and energy band change at the metal/semiconductor (M/S) region, which have been widely used to explain the response of NW or CNT gas sensors.[18,19,30−32] The chemical molecules adsorbed on the surface of the NWs can change the device's conductance, gate potential, local work function, band alignment, gate coupling, and carrier mobility, which are regarded as a "floating gate" effect on the conducting channel of the FETs.[30] Figure 5d (bottom image) presents a theoretical model to explain the floating gate effect on the performance of InAs NW photodetectors. The electrostatic interaction between chemical molecules and M/S contacts will increase the height of the energy band edge, thus prohibiting the carriers' injection and further decreasing the conductivity of InAs NW photodetectors. The peculiar electron accumulation layer and rich surface defect states of InAs NWs are responsible for the charge transfer to the adsorbed gas molecules.[19] Figure 5d (top image) shows the schematic of electron transfer from InAs NWs to the adsorbed chemical molecules. As a result, the carrier density decreased, as depicted in Figure 5c (blue line), and the carrier mobility also decreased (Figure 5e) due to scattering between carriers and adsorbed atmospheric molecules. The raised energy band edge also prohibited the injection of photon-generated electron−hole pairs into the S/D electrodes, thus decreasing the output

photocurrent. In addition, some photon-generated electron−hole pairs also transferred to the adsorbed atmospheric molecules, further reducing the photon-induced carrier density, as shown in Figure 5f (blue line).

Since the adsorption of atmospheric molecules can change the surface electron density and energy band of InAs NWs, metals with different work function are able to tune the electronic transport properties of InAs NWs. The inset of Figure 6a shows the sketch (top image) and TEM image (bottom image) of metal Au-cluster-decorated NW photodetectors and NWs. The Schottky junctions could form at the surface of InAs NWs due to the positive work function difference ($W_{Au}-W_{InAs}$). As a result, free electrons of InAs NWs are depleted, causing a lower on-current and positive shift in device threshold voltage (V_{th}), as depicted in Figure 6a (red line). Figure 6b shows the I_{ds} *versus* V_{ds} output characteristics of InAs NW photodetectors, indicating that the output current reduced with Au cluster. From the TEM image (Figure 6a, inset), it is found that the Au cluster is distributed uniformly on the surface of the NW (for more details on metal-cluster deposition, see Supporting Information). The photo-responsivity of metal Au-cluster-decorated InAs NW photodetectors (red line, Figure 6c) was much larger (∼300%) than that of the original one (blue line, Figure 6c). This is because the photogenerated electrons and holes are quickly driven toward the InAs NWs and metal Au cluster by the strong internal (built-in) electric fields, respectively, as shown in the energy band diagram of Figure 3b. Thus, the metal Au decoration can effectively depress the recombination rate of electron−hole pairs. Figure S5 (Supporting Information)
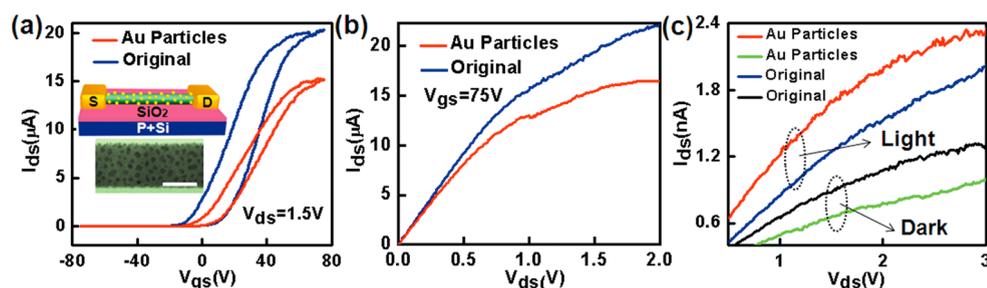
Figure 6. (a) I_{ds} *versus* V_{gs} transfer characteristics of the Au-cluster-decorated InAs NW photodetectors. The inset is the schematic and TEM image of 1 nm Au-cluster-decorated NW device and NWs. The scale bar is 30 nm. (b) I_{ds} *versus* V_{ds} output characteristics of the Au-cluster-decorated InAs NW photodetectors. (c) Photoinduced I_{ds} *versus* V_{ds} curves of the same detector.
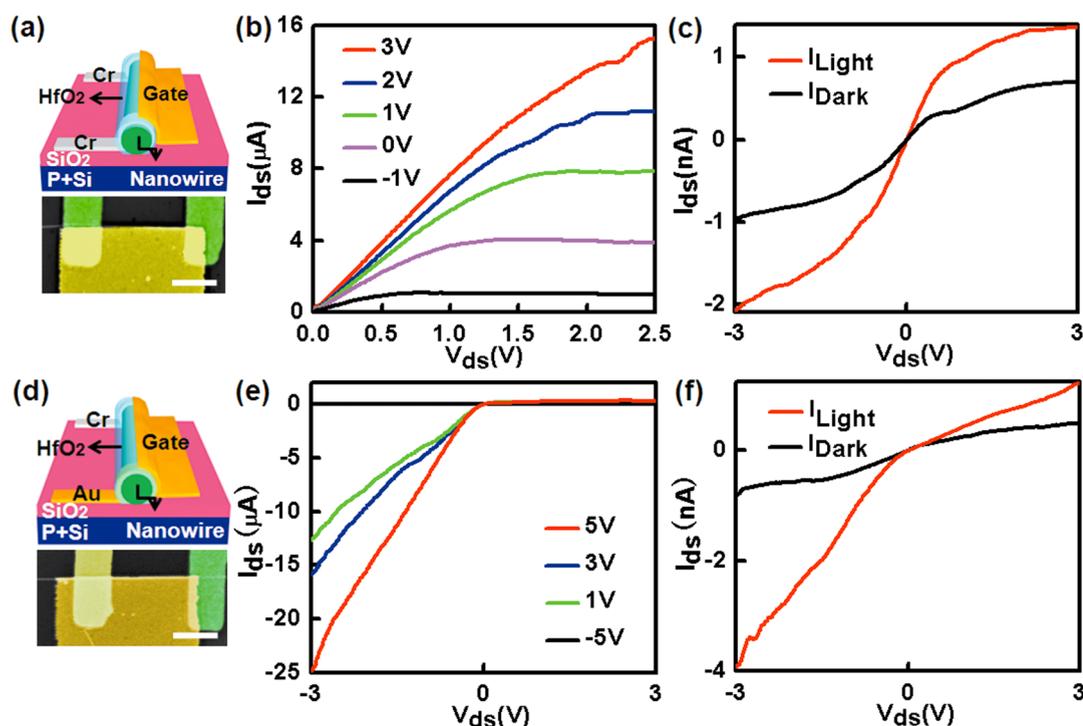

Figure 7. (a) Schematic and SEM image of half-wrapped top-gated Ohmic–Ohmic contacted InAs NW photodetectors. The scale bar is 1 μm. (b) I_{ds} *versus* V_{ds} curves of half-wrapped top-gated Ohmic–Ohmic contacted InAs NW photodetectors for various top-gated biases. (c) Photoinduced I_{ds} *versus* V_{ds} curves of the same photodetectors. (d) Schematic and SEM image of half-wrapped top-gated Schottky–Ohmic contacted InAs NW photodetectors. The scale bar is 1 μm. (e) I_{ds} *versus* V_{ds} curves of half-wrapped top-gated Schottky–Ohmic contacted InAs NW photodetectors for various top-gated biases. (f) Photoinduced I_{ds} *versus* V_{ds} curves of the same photodetectors. All of these measurements were conducted in the ambient atmosphere.

shows the effects of metal Cr cluster decoration on InAs NW photodetectors. The negative work function difference (W_{Cr}–W_{InAs}) induces a downward band-bending at the n-type InAs/Cr contacts; thus, free electrons are donated to InAs NWs. As a result, the on-current increases and the device V_{th} exhibits a negative shift.

In order to suppress the negative effects of atmospheric molecules and surface defect states, new photodetectors with a half-wrapped top-gate were successfully fabricated. The 10 nm HfO_2 gate dielectric was deposited *via* atomic layer deposition (ALD) technique. This type of photodetector geometry not only has a small parasitic capacitance and strong gate control effect but also could efficiently harvest the

light energy. Figure 7a shows the schematic (top image) and SEM image (bottom image) of a representative half-wrapped top-gated Ohmic–Ohmic contacted InAs NW photodetector. From the output characteristics (Figure 7b), we can find that the photodetectors had a good electrical property with a passivation layer and the top-gated biases could effectively control the carrier transport. Figure 7c presents the typical photoinduced I_{ds}–V_{ds} curve of the same device also indicating a good photoresponse in the ambient atmosphere. The schematic (top image) and SEM image (bottom image) of a representative Schottky–Ohmic contacted InAs NW photodetector with a half-wrapped top-gate are shown in Figure 7d. The drain current *versus* drain

voltage (I_{ds}–V_{ds}) output characteristics (Figure 7e) shows the good electrical performance of the half-wrapped top-gated Schottky−Ohmic contacted InAs NW photodetectors in the ambient atmosphere. The photoresponse in Figure 7f also confirms their good optoelectronic property.

CONCLUSIONS

In summary, this study reveals near-infrared photodetectors with high-performance optoelectronic properties based on the MBE-grown InAs NWs. The single InAs NW photodetectors have an impressive I_{on}/I_{off} ratio of 10^5 with a maximum field-effect mobility of ∼2000 cm^2/V·s. The photoresponsivity of Schottky−Ohmic contacted InAs NW photodetectors is ∼5.3 × 10^3 AW^{-1}, which is ∼300% larger than the Ohmic−Ohmic contacted devices (∼1.9 × 10^3 AW^{-1}). We also studied the effects of atmospheric molecules, HfO$_2$ passivation layer, and metal-cluster decoration on the photoresponse of InAs NW photodetectors. It is shown that the adsorbed atmospheric molecules can reduce the current density, which is attributed to the charge transfer and electrostatic interaction between InAs NWs and atmospheric molecules. Additionally, the metal Au cluster decoration could increase the photoresponsivity by ∼300%, which is due to the formation of Schottky junctions at InAs/Au cluster contacts. To suppress the negative effects of atmospheric molecules and surface defect states, for the first time, half-wrapped top-gated InAs NW photodetectors were introduced in this paper. These interesting nanoscale infrared photodetectors may provide potential applications in photonics, electronics, and their integrated systems.

METHODS

InAs NWs Synthesis. The InAs NWs used in this work were synthesized on GaAs (111)$_B$ substrates in a Riber 32 MBE system by the Au-catalyzed vapor−liquid−solid (VLS) growth mechanism. The substrate surface was first deoxidized at 630 °C for 15 min followed by growing a 300 nm GaAs buffer layer to obtain a smooth surface. Then, the prepared substrate was transferred to the MBE preparation chamber. An ultrathin Au film was then deposited on it from the Knudsen cell at room temperature. Subsequently, the Au-covered GaAs substrate was transferred back to the growth chamber and annealed for 5 min at 550 °C in an As$_4$ ambient atmosphere to form gold droplets. Finally, the indium source was used to grow InAs NWs at 350 °C. Both the indium and As$_4$ fluxes were controlled by beam equivalent pressure (BEP). The indium/As$_4$ BEP ratio was set at 1:20, and the growth time was 90 min. After the growth, the indium source was switched off and the substrate was cooled under As$_4$ overpressure to 300 °C. Finally, the substrates were cooled to room temperature naturally.

Photodetector Fabrication and Characterization. The InAs NWs were transferred to precleaned P$^+$-Si/SiO$_2$ (300 nm) substrates, followed by spin-coated MMA and PMMA. Then electron-beam lithography (JEOL 6510 with NPGS System) was used to define the S/D patterns. Before metallization, the NWs were dipped into a 2% HF solution for 15 s to remove the native oxide (for more details, see Supporting Information). The Ohmic−Ohmic contacted NW photodetectors employed Cr/Au (20 nm/40 nm) as S/D electrodes; the Schottky−Ohmic contacted NW photodetectors employed Cr/Au (20 nm/40 nm) and Au (60 nm) as S/D electrodes, respectively. Optoelectronic measurements of InAs NW photodetectors were performed with the Lake Shore TTPX Probe Station with Agilent 4155C semiconductor parameter analyzer.

Conflict of Interest: The authors declare no competing financial interest.

Supporting Information Available: Procedures of metal-cluster deposition on InAs NW photodetectors; methods for determining the optimized time of native oxide layer etch; photoluminescence (PL) spectrum of InAs NWs (Figure S1); top-gated Ohmic−Ohmic contacted InAs NW photodetectors (Figure S2); top-gated Schottky−Ohmic contacted InAs NW photodetectors (Figure S3); photoresponse of InAs NW array FETs to various gases, such as O$_2$ and N$_2$ molecules (Figure S4); effects of metal Cr cluster decoration on electrical properties of InAs NW photodetectors (Figure S5). This material is available free of charge *via* the Internet at http://pubs.acs.org.

REFERENCES AND NOTES

1. Takahashi, T.; Takei, K.; Adabi, E.; Fan, Z. Y.; Niknejad, A. M.; Javey, A. Parallel Array InAs Nanowire Transistors for Mechanically Bendable, Ultrahigh Frequency Electronics. *ACS Nano* **2010**, *4*, 5855–5860.

2. Ford, A. C.; Ho, J. C.; Chueh, Y. L.; Tseng, Y. C.; Fan, Z. Y.; Guo, J.; Bokor, J.; Javey, A. Diameter-Dependent Electron Mobility of InAs Nanowires. *Nano Lett.* **2009**, *9*, 360–365.

3. Han, N.; Wang, F. Y.; Hou, J. J.; Yip, S. P.; Lin, H.; Xiu, F.; Fang, M.; Yang, Z. X.; Shi, X. L.; Dong, G. F.; *et al.* Tunable Electronic Transport Properties of Metal-Cluster-Decorated III–V Nanowire Transistors. *Adv. Mater.* **2013**, *25*, 4445–4451.

4. Wahl, R. E.; Wang, F. Y.; Chung, H. E.; Kunnen, G. R.; Yip, S. P.; Lee, E. H.; Pun, E. Y. B.; Raupp, G. B.; Allee, D. R.; Ho, J. C. Stability and Low-Frequency Noise in InAs NW Parallel-Array Thin-Film Transistors. *IEEE Electron Device Lett.* **2013**, *34*, 765–767.

5. Thelander, C.; Froberg, L. E.; Rehnstedt, C.; Samuelson, L.; Wernersson, L. E. Vertical Enhancement-Mode InAs Nanowire Field-Effect Transistor with 50-nm Wrap Gate. *IEEE Electron Device Lett.* **2008**, *29*, 206–208.

6. Xia, H.; Lu, Z. Y.; Li, T. X.; Parkinson, P.; Liao, Z. M.; Liu, F. H.; Lu, W.; Hu, W. D.; Chen, P. P.; Xu, H. Y.; *et al.* Distinct Photocurrent Response of Individual GaAs Nanowires Induced by n-Type Doping. *ACS Nano* **2012**, *6*, 6005–6013.

7. Dong, Y. J.; Tian, B. Z.; Kempa, T. J.; Lieber, C. M. Coaxial Group III-Nitride Nanowire Photovoltaics. *Nano Lett.* **2009**, *9*, 2183–2187.

8. Gudiksen, M. S.; Lauhon, L. J.; Wang, J. F.; Smith, D. C.; Lieber, C. M. Growth of Nanowire Superlattice Structures for Nanoscale Photonics and Electronics. *Nature* **2002**, *415*, 617–620.

9. Chen, R. S.; Chen, H. Y.; Lu, C. Y.; Chen, K. H.; Chen, C. P.; Chen, L. C.; Yang, Y. J. Ultrahigh Photocurrent Gain in m-Axial GaN Nanowires. *Appl. Phys. Lett.* **2007**, *91*, 223106.

10. Gallo, E. M.; Chen, G. N.; Currie, M.; McGuckin, T.; Prete, P.; Lovergine, N.; Nabet, B.; Spanier, J. E. Picosecond Response Times in GaAs/AlGaAs Core/Shell Nanowire-Based Photodetectors. *Appl. Phys. Lett.* **2011**, *98*, 241113.

11. Jiang, X. C.; Xiong, Q. H.; Nam, S.; Qian, F.; Li, Y.; Lieber, C. M. InAs/InP Radial Nanowire Heterostructures as High Electron Mobility Devices. *Nano Lett.* **2007**, *7*, 3214–3218.

12. Dayeh, S. A.; Aplin, D. P. R.; Zhou, X. T.; Yu, P. K. L.; Yu, E. T.; Wang, D. L. High Electron Mobility InAs Nanowire Field-Effect Transistors. *Small* **2007**, *3*, 326–332.

13. Schroer, M. D.; Petta, J. R. Correlating the Nanostructure and Electronic Properties of InAs Nanowires. *Nano Lett.* **2010**, *10*, 1618–1622.

14. Mead, C. A.; Spitzer, W. G. Fermi Level Position at Semiconductor Surfaces. *Phys. Rev. Lett.* **1963**, *10*, 471–472.

15. van Schilfgaarde, M.; Weber, E. R.; Newman, N. Pressure Dependence of III–V Schottky Barriers: A Critical Test of Theories for Fermi Level Pinning. *Phys. Rev. Lett.* **1994**, *73*, 581–584.

16. Chen, Y.; Hermanson, J. C.; Lapeyre, G. J. Coupled Plasmon and Phonon in the Accumulation Layer of InAs (110) Cleaved Surfaces. *Phys. Rev. B* **1989**, *39*, 12682–12687.

17. Noguchi, M.; Hirakawa, K.; Ikoma, T. Intrinsic Electron Accumulation Layers on Reconstructed Clean InAs (100) Surfaces. *Phys. Rev. Lett.* **1991**, *66*, 2243–2246.

18. Offermans, P.; Crego-Calama, M.; Brongersma, S. H. Gas Detection with Vertical InAs Nanowire Arrays. *Nano Lett.* **2010**, *10*, 2412–2415.

19. Du, J.; Liang, D.; Tang, H.; Gao, X. P. A. InAs Nanowire Transistors as Gas Sensor and the Response Mechanism. *Nano Lett.* **2009**, *9*, 4348–4351.

20. Zhou, X.; Dayeh, S. A.; Aplin, D.; Wang, D.; Yu, E. T. Direct Observation of Ballistic and Drift Carrier Transport Regimes in InAs Nanowires. *Appl. Phys. Lett.* **2006**, *89*, 053113.

21. Chuang, S.; Gao, Q.; Kapadia, R.; Ford, A. C.; Guo, J.; Javey, A. Ballistic InAs Nanowire Transistors. *Nano Lett.* **2013**, *13*, 555–558.

22. Sun, M. H.; Joyce, H. J.; Gao, Q.; Tan, H. H.; Jagadish, C.; Ning, C. Z. Removal of Surface States and Recovery of Band-Edge Emission in InAs Nanowires through Surface Passivation. *Nano Lett.* **2012**, *12*, 3378–3384.

23. Chueh, Y. L.; Ford, A. C.; Ho, J. C.; Jacobson, Z. A.; Fan, Z. Y.; Chen, C. Y.; Chou, L. J.; Javey, A. Formation and Characterization of Ni$_x$InAs/InAs Nanowire Heterostructures by Solid Source Reaction. *Nano Lett.* **2008**, *8*, 4528–4533.

24. Chen, S. Y.; Wang, C. Y.; Ford, A. C.; Chou, J. C.; Wang, Y. C.; Wang, F. Y.; Ho, J. C.; Wang, H. C.; Javey, A.; Gan, J. Y.; *et al.* Influence of Catalyst Choices on Transport Behaviors of InAs NWs for High-Performance Nanoscale Transistors. *Phys. Chem. Chem. Phys.* **2013**, *15*, 2654–2659.

25. Lind, E.; Persson, A. I.; Samuelson, L.; Wernersson, L. E. Improved Subthreshold Slope in an InAs Nanowire Heterostructure Field-Effect Transistor. *Nano Lett.* **2006**, *6*, 1842–1846.

26. Ford, A. C.; Ho, J. C.; Fan, Z. Y.; Ergen, O.; Altoe, V.; Aloni, S.; Razavi, H.; Javey, A. Synthesis, Contact Printing, and Device Characterization of Ni-Catalyzed, Crystalline InAs Nanowires. *Nano Res.* **2008**, *1*, 32–39.

27. Ahn, Y.; Dunning, J.; Park, J. Scanning Photocurrent Imaging and Electronic Band Studies in Silicon Nanowire Field Effect Transistors. *Nano Lett.* **2005**, *5*, 1367–1370.

28. Hu, Y. F.; Chang, Y. L.; Fei, P.; Snyder, R. L.; Wang, Z. L. Designing the Electric Transport Characteristics of ZnO Micro/Nanowire Devices by Coupling Piezoelectric and Photoexcitation Effects. *ACS Nano* **2010**, *4*, 1234–1240.

29. Huang, M. L.; Chang, Y. C.; Chang, C. H.; Lee, Y. J.; Chang, P.; Kwo, J.; Wu, T. B.; Hong, M. Surface Passivation of III–V Compound Semiconductors Using Atomic-Layer-Deposition-Grown Al$_2$O$_3$. *Appl. Phys. Lett.* **2005**, *87*, 252104.

30. Pan, C. F.; Yu, R. M.; Niu, S. M.; Zhu, G.; Wang, Z. L. Piezotronic Effect on the Sensitivity and Signal Level of Schottky Contacted Proactive Micro/Nanowire Nanosensors. *ACS Nano* **2013**, *7*, 1803–1810.

31. Niu, S. M.; Hu, Y. F.; Wen, X. N.; Zhou, Y. S.; Zhang, F.; Lin, L.; Wang, S. H.; Wang, Z. L. Enhanced Performance of Flexible ZnO Nanowire Based Room-Temperature Oxygen Sensors by Piezotronic Effect. *Adv. Mater.* **2013**, *25*, 3701–3706.

32. Heinze, S.; Tersoff, J.; Martel, R.; Derycke, V.; Appenzeller, J.; Avouris, P. Carbon Nanotubes as Schottky Barrier Transistors. *Phys. Rev. Lett.* **2002**, *89*, 106801.

33. Liu, Z.; Chen, G.; Liang, B.; Yu, G.; Huang, H. T.; Chen, D.; Shen, G. Z. Fabrication of High-Quality ZnTe Nanowires toward High-Performance Rigid/Flexible Visible-Light Photodetectors. *Opt. Express* **2013**, *21*, 7799–7810.

34. Chen, G.; Liang, B.; Liu, X.; Liu, Z.; Yu, G.; Xie, X. M.; Luo, T.; Chen, D.; Zhu, M. Q.; Shen, G. Z.; *et al.* High-Performance Hybrid Phenyl-C61-Butyric Acid Methyl Ester/Cd$_3$P$_2$ Nanowire Ultraviolet−Visible−Near Infrared Photodetectors. *ACS Nano* **2014**, *8*, 787–796.

35. Moon, T. H.; Jeong, M. C.; Oh, B. Y.; Ham, M. H.; Jeun, M. H.; Lee, W. Y.; Myoung, J. M. Chemical Surface Passivation of HfO$_2$ Films in a ZnO Nanowire Transistor. *Nanotechnology* **2006**, *17*, 2116–2121.

36. Kim, S.; Carpenter, P. D.; Jean, R. K.; Chen, H.; Zhou, C. W.; Ju, S.; Janes, D. B. Role of Self-Assembled Monolayer Passivation in Electrical Transport Properties and Flicker Noise of Nanowire Transistors. *ACS Nano* **2012**, *6*, 7352–7361.

37. Zou, X. M.; Liu, X. Q.; Wang, C. L.; Jiang, Y.; Wang, Y.; Xiao, X. H.; Ho, J. C.; Li, J. C.; Jiang, C. Z.; Xiong, Q. H.; *et al.* Controllable Electrical Properties of Metal-Doped In$_2$O$_3$ Nanowires for High-Performance Enhancement-Mode Transistors. *ACS Nano* **2013**, *7*, 804–810.